ACS APPLIED MATERIALS & INTERFACES

www.acsami.org

Research Article

Enhanced Room-Temperature Ionic Conductivity of $NaCB_{11}H_{12}$ via High-Energy Mechanical Milling

Fabrizio Murgia, Matteo Brighi, Laura Piveteau, Claudia E. Avalos, Valerio Gulino, Marc C. Nierstenhöfer, Peter Ngene, Petra de Jongh, and Radovan Černý*

Cite This: https://doi.org/10.1021/acsami.1c21113

Read Online

ACCESS | Metrics & More | Article Recommendations | Supporting Information

ABSTRACT: The body-centered cubic (bcc) polymorph of $NaCB_{11}H_{12}$ has been stabilized at room temperature by high-energy mechanical milling. Temperature-dependent electrochemical impedance spectroscopy shows an optimum at 45-min milling time, leading to an rt conductivity of 4 mS cm^{-1}. Mechanical milling suppresses any order−disorder phase transition in the investigated temperature range. Nevertheless, two main regimes can be identified, with two clearly distinct activation energies. Powder X-ray diffraction and ^{23}Na solid-state NMR reveal two different Na^+ environments, which are partially occupied, in the bcc polymorph. The increased number of available sodium sites w.r.t. ccp polymorph raises the configurational entropy of the bcc phase, contributing to a higher ionic conductivity. Mechanical treatment does not alter the oxidative stability of $NaCB_{11}H_{12}$. Electrochemical test on a symmetric cell (Na|$NaCB_{11}H_{12}$|Na) without control of the stack pressure provides a critical current density of 0.12 mA cm^{-2}, able to fully charge/discharge a 120 mA h g^{-1} specific capacity positive electrode at the rate of $C/2$.

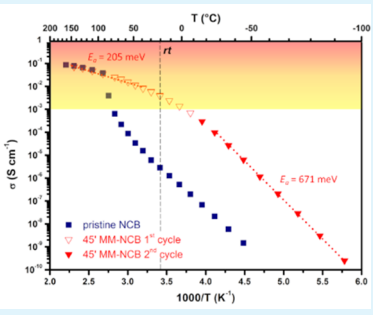

KEYWORDS: *mechanical milling, Na^+ superionic conductor, $NaCB_{11}H_{12}$, solid electrolyte, hydroborate, boron chemistry*

1. INTRODUCTION

In the search for safer and more efficient electrochemical energy storage systems, Na-based all-solid-state batteries (Na-ASSBs) represent a viable evolution from the current Li-ion technology. Na-ASSBs combine the advantages of availability and low cost of Na precursors,[1,2] with both intrinsic enhanced safety and extended temperature operating range offered by the nonflammable solid electrolyte (SE) compared to lithium-ion batteries.[3−6] Moreover, they enable the use of metallic sodium as negative electrode,[7] thus potentially meeting the requirement of high volumetric (>750 Wh L^{-1}) and gravimetric (>350 Wh kg^{-1}) energy densities,[8] which are beyond current lithium-ion batteries (LIBs).[9] Finally, their production can skip several conditioning steps needed for the fabrication of conventional cells, thus reducing costs, as already shown for Li-based counterparts.[10,11] The challenge for Na-ASSBs has been mainly the development of room-temperature (rt) fast ion conductors that withstand elevated current densities. In the past years, both Li- and Na-based solid ionic conductors have been developed that rival, and in some cases beat, the ionic conductivity of current liquid electrolytes.[12−15] Other drawbacks plaguing SSBs that need to be urgently tackled are the narrow electrochemical voltage window,[7] limited chemomechanical stability,[6,16] poor compatibility with electrodes,[17,18] and a thorough determination of the stack pressure.[19,20] Focusing on Na-ion conductors, several classes of chemical compounds acting as SEs have been investigated, e.g., β-Al_2O_3 and NASICON, that despite their good chemical stability require harsh synthesis conditions and suffer from poor electrode contact at rt;[6] sulfide-based compounds, such as thiophosphates (cubic Na_3PS_4,[21] $Na_{11}Sn_2PS_{12}$[13]), and P-replacing derivatives Na_3SbS_4,[22] although being softer and more easily processable, provide limited electrochemical stability.[23,24] Furthermore, an emerging class of antiperovskites,[25] with general formula Na_3OX (X = Cl, Br, I, BH_4) is less prone to oxidation, but their compatibility with metal anode and their conductivity[26] are still a matter of discussion.

Thanks to their low density, low toxicity, and soft mechanical properties, complex hydrides have gained particular attention as SEs, both on Li-[27] and post Li-based systems.[28] In particular, hydroborates with large cluster anions, $[B_xH_x]^{2-}$ (x = 10, 12), and their C-derivatives $[CB_{x-1}H_x]^-$ show enhanced oxidative stability with respect to smaller complex hydrides,[29,30] due to the strong electronic delocalization among their cages.[31] Moreover, reports dealing with their compatibility with metallic Na,

Received: November 1, 2021
Accepted: December 8, 2021

ACS Publications © XXXX American Chemical Society

thermal stability,[32] and low area-specific resistance[33] confirm their possible use as electrolytes for next-generation ASSBs.[34] The cation motion is strongly related to the physicochemical properties of the polyhedral anions. Owing to relatively large size and high symmetry, these anions form crystal structures in which their packing provides a wide number of cation vacant sites, as well as a low charge-to-volume ratio, and thus are among the weakest coordinating anions.[35] In addition, many theoretical[36−38] and experimental[39−41] studies pointed out the relationship between the anion rotation rates and the cation diffusivity in these rotatory phases (plastic crystals).[42] Moreover, in the case of carba-*closo* cages, the C-substitution perturbs the local coulombic interaction by withdrawing electronic density from the C−H bond, which further enhances the cation repulsion.[38] Na^+ fast conductivity in such systems is driven by an order−disorder phase transition, which generally occurs above rt. Lowering the transition temperature, i.e., frustrating the energy landscape of the anionic lattice, is of paramount importance to get SEs that can operate at rt. It emerges that such destabilization can be induced using various strategies: atom deficiency,[43] anion substitution,[44] anion mixing,[45] composite formation,[46] and nanoconfinement.[47] Mechanical milling (MM) is also a well-established technique to provide energy perturbation in a solid, diminishing average crystallite sizes, as well as stabilizing nonequilibrium phases in various materials.[48,49] Repeated collisions between powder and grinding milling tools (spheres, vial) provide mechanical stress, leading to the accumulation of structural defects,[50,51] such as cation site disorder,[52] or shear and tear, which can result in distorted coordination geometries.[53] The effect of mechanical treatment depends on a number of parameters, such as milling time, geometry and motion of the vial, materials of the colliding elements, etc., which can influence either the physical or chemical properties of the milled sample.[54−57] On this basis, mechanical milling has been considered a promising technique to suppress the order−disorder phase transition in both lithium[58] and sodium *closo*-borates: in particular, Tang et al. reported that the crystallite size reduction and the introduction of defects generated by ball-milling in $Na_2B_{12}H_{12}$ stabilized the Na-conducting phase at rt.[59] The same work also reported the mechanical milling of $NaCB_{11}H_{12}$ (hereafter NCB), which crystallizes at rt in an ordered orthorhombic ($Pca2_1$) deformation of a cubic face-centered cell (fcc) of disordered ht-phase with cubic close packing (ccp) of anions. Moreover, a partial formation of the ht-phase has been claimed. However, no further ionic conductivity measurements were provided. In the present study, we report the stabilization at rt of the cubic body-centered (bcc) polymorph of NCB via high-energy mechanical milling. Such metastable phase provides fast Na^+ conduction at rt. To shed light on the reasons of the increased conductivity, the combination of the conductivity measurements as a function of milling time and the structural model of the pristine and milled NCB will be discussed. Finally, to foresee further applications of MM-NCB as an SE, its electrochemical oxidative stability and ability to allow fast and safe (i.e., without dendrite penetration) Na^+ shuttling were investigated.

2. EXPERIMENTAL SECTION

2.1. Synthesis. $NaCB_{11}H_{12}$ (NCB) was purchased from KatChem Ltd. (Czech Republic). Prior to use, it was dried at 180 °C under dynamic vacuum for 12 h. Subsequently, it underwent high-energy ball-milling in an 8000M Mixer-Mill (Spex) for selected milling times, laying between 15 min and 6 h. In a typical preparation, a Fe−Cr stainless-steel jar is poured with spheres of the same material, and 110 mg of dried powder. The ball-to-powder weight ratio is set to 180. Such a mill performs a three-dimensional (3D) motion, which results from the combination of a shaking and a periodic movement describing a figure-eight loop.

X-ray powder diffraction (XPD) patterns were collected using an Empyrean (Panalytical) diffractometer (Cu Kα) in Debye−Scherrer geometry, equipped with a PIXcell3D detector. The MM-NCB structure was solved with the software FOX,[60] whereas Rietveld refinements were performed using the software TOPAS.[61] Scanning electron microscopy (SEM) was used to analyze the surface morphology (Zeiss LEO-1455 VP), equipped with both secondary emission and back-scattered electron detectors. The samples underwent air exposure (less than 5 s) during loading into the SEM. DSC analysis: a Mettler Toledo HP DSC 1-STAR differential scanning calorimeter was used to analyze the thermal stability of the samples. About 5−10 mg of the sample was placed into closed aluminum crucibles (40 mL) with a lid inside a glovebox. The samples were heated and cooled in the desired temperature range at 10 °C min^{-1} under an Ar flow of 10 mL min^{-1}. Diffuse reflectance infrared Fourier transform spectroscopy (DRIFTS) measurements were performed on a PerkinElmer 2000 spectrometer. In the glovebox, the samples have been placed in an airtight sample holder, with KBr windows. Spectra were acquired in the 3200−900 cm^{-1} range with a resolution of 4 cm^{-1}. Reported data are an average of 32 scans. Raman spectra were collected at rt using a Horiba LabRAM HR Evolution spectrometer with an excitation wavelength of 532 nm and the resolution of 2 cm^{-1} over the full wavenumber range. The laser light was focused on a 2 μm spot using a window-corrected 63× objective. To avoid H_2O contamination, each sample was measured inside a 0.5 mm diameter quartz capillary (thickness = 0.01 mm), sealed in glovebox.

Solid-state ^{23}Na NMR spectra were recorded on a 900 MHz Bruker spectrometer (21.1 T) equipped with an Avance Neo console and a 3.2 mm three-channel low-temperature magic-angle spinning probe. Samples were packed into 3.2 mm zirconia rotors in a glovebox and spun up to 24 kHz spinning speed using dry nitrogen gas. Spectra were acquired at temperatures of 300 and 360 K, which were achieved using a Bruker BCUII temperature control unit. All spectra were acquired using a Hahn echo pulse sequence with $\pi/4$ pulse of 4.5 μs, an echo delay of τ = 41.6 μs, and four accumulated transients. Recycle delays were set to five times T_1 for all samples, which all exhibited a distribution of relaxation times $\ll$1 s. ^{23}Na chemical shifts were referenced to NaCl (s) (7.21 ppm) at 12.5 kHz MAS.[62]

The temperature-dependent ionic conductivity was studied by electrochemical impedance spectroscopy (EIS). Typically, 100 mg of powder was placed into a stainless-steel cylindrical dye (10 mm diameter), covered on both sides by a conductive carbon layer, and subsequently compacted undergoing a uniaxial pressure of 240 MPa, by means of a hydraulic press. The final thickness of the pellet is around 0.5 mm. The thin carbon layer on each side of the pellet was added to minimize the interfacial resistance. EIS measurements were carried out using an SP-200 (BioLogic), in a range of frequencies from 10^{-2} to 7 × 10^7 Hz, with an AC perturbation signal of 10 mV. The temperature control was realized via a nitrogen stream in a Novocool (Novocontrol) temperature controlling system. EIS spectra were collected in subsequent steps of 10 or 20 °C from −100 to 180 °C. Electrochemical oxidative stability was studied by slow-scan rate cyclic voltammetry (SSRCVs) at a scan speed of 50 μV s^{-1}. A typical setup features a two-electrode cell, made with a 3/4″ PFA body (Swagelok), a glassy carbon disk (Sigradur, 180 μm thickness, HTW) as the working electrode (WE) and a freshly polished sodium disk as the counter and reference electrodes (CE/RE). These disks sandwich the investigated sample, whose pelletizing procedure is described in detail elsewhere.[32] The mix of the upper SE layer with a carbonaceous material increases the surface contact between SE and WE, thus enhancing the signals coming from oxidation reactions. Critical current density (CCD) measurement on the MM sample was performed with an analogous setup, only replacing the glassy carbon electrode with a second sodium disk. SSRCV and CCD were both performed at rt. All of the pellet preparation and cell

https://doi.org/10.1021/acsami.1c21113
ACS Appl. Mater. Interfaces XXXX, XXX, XXX−XXX

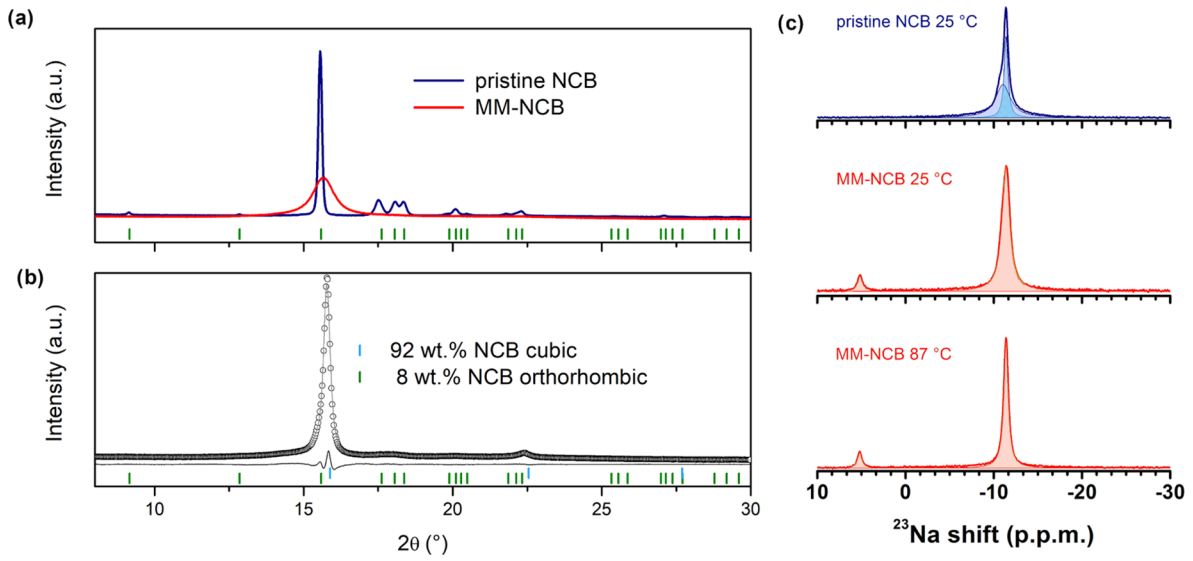

Figure 1. (a) XPD of the pristine NCB (blue line), the 45-min MM-NCB (red line), and peak position of orthorhombic NCB (green bars). (b) Rietveld refinement plot of 45-min milled sample (after DSC—10 °C min^{-1} up to 250 °C), composed of two phases, the main one being the bcc polymorph (light blue bars). However, a small amount of pristine orthorhombic phase is still present (green bars). (c) ^{23}Na SS−NMR spectra of pristine (blue line) and 45-min MM-NCB (red line). The bcc polymorph stabilized by MM shows two distinct Na signals (5.2 and −11.4 ppm, respectively), as a consequence of two different Na^+ environments, the former where Na^+ is in triangular coordination, the latter in which Na is slightly shifted from the center of a tetrahedron (cf. Figure S6).

assembly were carried out in an Ar-filled glovebox, whose O_2 and H_2O levels are both kept below 0.1 ppm.

3. RESULTS AND DISCUSSION

f1 Figure 1a gathers the XPD patterns of the pristine (blue) and the mechanically milled (red) NCB, respectively. After 45 min of MM, no bumps arising from the background supporting the formation of an amorphous phase are noticeable. Nonetheless, the signature due to the pristine sample (orthorhombic cell) is almost completely lost, with the unique exception of the main (111) reflection (2θ = 15.6°), which shows a large broadening. Such evidence is compatible with the reduction of the crystalline domains and/or introduction of local strain (microstrain) (Figures S1 and S2) driven by the MM. More interestingly, Rietveld refinement on the further recrystallized sample (Figure 1b) reveals that MM-NCB is mainly composed of a new bcc phase of NCB (s.g *Im*3*m*; *a* = 7.882 Å), flanked by an orthorhombic NCB. Also solid-state NMR, which is more sensitive to short-range structures, confirms the formation of a different arrangement in MM-NCB after ball-milling compared to the initial NCB material (Figure 1c). Indeed, the solid-state ^{23}Na NMR spectrum of pristine NCB (blue) shows one main peak centered at −11.4 ppm, which arises from the convolution of two close signals, standing for two similar Na^+ environments in the orthorhombic phase. By contrast, MM-NCB features two distinct signals, the less intense at 5.2 ppm whereas a stronger one at −11.4 ppm, with 0.09 being the ratio between the two peak areas. This indicates the presence of two different Na^+ environments in the bcc polymorph. Interestingly, the positions and the ratio between the two peaks remain constant when heating from rt to 87 °C, indicating that the chemistry and the occupancy of each site are not significantly affected by the temperature increase. However, there is a slight decrease of the peaks' widths with increasing temperature, which could indicate that their shape is dominated by mobility or dynamics.

This cubic phase is different from the ht disordered polymorph reported by Tang et al.,[63] where the $[CB_{11}H_{12}]^-$ anions are packed in an fcc sublattice. Although the coexistence of different polymorphs has been already reported for *closo*-borates far from rt,[64] the only evidence of a bcc arrangement on NCB can be found in the same work of Tang et al.,[63] where in a diffractogram collected at 428 K (155 °C), a peak has been tentatively assigned to a bcc phase. Interestingly, this peak disappeared in a next pattern, although at the same temperature, collected for a longer time. In contrast, in the present work, the bcc phase has been stabilized at rt and does not undergo further phase transition toward the starting orthorhombic polymorph after being cooled down to rt (Figure 1b), as also confirmed by the DSC measurement (Figure S3). This is not uncommon for MM treatments, which can promote phase transitions, quenching metastable phases under ambient conditions.[53,65] Finally, even though a systematic study on the parameters affecting the formation of metastable bcc-NBC is out of the scope of this work, it is important to underline that the success on the stabilization of such polymorph at rt is due to the use of a 3D mill. As mentioned above, the attempt to stabilize conductive phases of NCB at rt via planetary ball-milling led, after 86 h of milling time, only to the partial formation of fcc phase,[59] in contrast to 30 min to start forming bcc phase via 3D milling (Figure S1). Hence, different milling conditions, such as more energetic mechanical milling provided by 3D mill,[48,66] can affect the polymorphism and eventually drive the stabilization of less common crystalline phases, as already shown for other systems, in both organic and inorganic structures.[67,68]

Figure 2 reports the DC conductivity of MM-NCB as a function of inverse temperature. In contrast to the pristine sample, where the conductivity jumps at around 83 °C because of an order−disorder phase transition, for MM-NCB, this is no longer noticeable. Such evidence results from the stabilization of the bcc conductive polymorph of NCB via MM, which shows a conductivity of 4 mS cm^{-1} at rt. Therefore MM-NCB ranks as one of the fastest Na^+ conductors among hydroborates. Alternative causes for such an improvement in conductivity are excluded for the following reasons. First, a size reduction

https://doi.org/10.1021/acsami.1c21113
ACS Appl. Mater. Interfaces XXXX, XXX, XXX−XXX

effect, that is a direct consequence of the MM treatment, cannot be the cause of the improved ionic conductivity since a clear recrystallization effect was observed by XPD already above 140 °C (Figure S4) and the Na^+ conductivity is perfectly reproducible after two cycles between −100 and 160 °C. In addition, also an effect related to conductive grain boundaries, or conductive interfaces, must be excluded. Indeed, even if it was observed for other hydroborates, such as $LiBH_4$,[69] a conductive or resistive contribution from grain boundaries was never observed for *closo*-borates. The superionic regime is kept down to −10 °C, thus providing a wide operational range for further Na-based SSBs. Although from calorimetry (Figure S3), there is no trace of any further phase transition in the investigated range of temperature, MM-NCB's conductivity shows a non-Arrhenius behavior. This can be read as a continuous change connecting two Arrhenius-like regions, above and below rt, where the activation energies amount to 205 and 671 meV, respectively.

Interestingly, both values are comparable to those observed for the pristine NCB, before and after its order−disorder phase transition. Above the transition temperature shown by NCB, as well as other *closo*- and carba-*closo*-borates, the thermal energy is sufficiently high to allow anion rotation, thus promoting the cation mobility independently from their lattice packing, cage shape and heteroatom substitution, as it possible to argue by comparing, for instance, the conductivities of the ht-polymorphs of $Na_2B_{12}H_{12}$ (bcc)[64] with $NaCB_9H_{10}$ (hexagonal).[70] Moreover, nonmilled NCB itself shows a rich polymorphism above its order−disorder phase transition temperature, but no further jumps of the conductivity are noticeable accordingly.[63] At lower temperatures, despite a little hysteresis (nevertheless observed for all *closo*- and carba-*closo*-borates) probably due to the anion dynamic inertia, below 40 °C, the activation energy of the ordered orthorhombic phase amounts to 629 meV.

Peculiarly, in the disordered bcc phase, the activation energy is 671 meV, regardless of the different anion sublattice. Hence, when the temperature decreases, during the siding, the ion dynamic slows down while the high-symmetry structure is preserved, quenched in a metastable phase. This fact is at the origin of the improved Na conductivity and likely lies in the augmented entropy provided by the bcc anion arrangement. Indeed, writing the Arrhenius relation as $\sigma T = \sigma_0 e^{-E_a/k_B T}$, the entropic term is encompassed in the preexponential factor. σ_0 is a function of parameters that are structure-related (details in the Supporting Information) and depends exponentially on the system entropy.

Assuming that structural and chemical parameters (such as cation concentration, mean square jumping distance, and attempt jump frequency) do not change over several orders of magnitude between pristine and MM-NCB, the difference of $\ln(\sigma_0)$ should only result from the entropy difference existing between these two polymorphs. In this work, the difference of $\ln(\sigma_0)$ (σ_0 in S cm^{-1}) between pristine and MM-NCB amounts to 11.25.

This value is comparable to other NASICON- and thiophosphates-type ionic conductors, where S_m is about 8−12 k_B.[71,72] One contribution to the migration entropy is surely of configuration nature. This was previously investigated by Kweon et al. for $Li_2B_{12}H_{12}$ and $Na_2B_{12}H_{12}$ analyzing the contribution of partial occupation between available interstitial sites for mobile cations (linear, trigonal, and tetrahedral coordination).[73] In our case, the difference is between a completely ordered situation (orthorhombic NCB) where Na completely fills off-centered octahedral sites, and a disordered bcc structure (MM-NCB). To calculate the configurational entropy of the latter, we relied on a structural model proposed for a similar compound and revised as shown in Figure S6. The model is based on the structure proposed by Brighi et al.[32] for $Na_3(CB_{11}H_{12})(B_{12}H_{12})$ modified according to results of the NMR spectroscopy pointing to two sodium sites in the structure. The modified model corresponds to the model of ht-AgI, i.e., one cation in the triangular 24h Wyckoff site and the other in the tetrahedral 12d site. In the case of MM-NCB, the second cation (Na2) lying in the 24g site, is off-centered inside the tetrahedron. Constraining the total Na occupancy to converge to two atoms for unit cell, the ratio of Na1/Na2 occupancy (triangular/tetrahedral) amounts to 0.11, in fair agreement with NMR results mentioned above, which capture the mobility averaged chemical surroundings of the Na atoms on the NMR timescale. The calculation was conducted following the model reported by Kweon et al., and, in this case, amounts to $3.75/k_B$. The calculated value roughly corresponds to 1/3 of the total measured entropy difference. Obviously, a deeper investigation with molecular dynamic simulation can help to obtain a more realistic value: indeed, this contribution alone is not enough to fully explain the entropy difference between the two compounds. The residual quantity could be attributed to a vibrational term resulting from a different phonon mode; therefore, the measurement and the simulation of the phonon density of state is subject of the current investigation. Nevertheless, this corroborates the hypothesis that in both phases at low temperatures, the anion dynamic plays a similar role in the conduction process, indeed preserving the same activation energy for diffusion. Contrasting is the structure itself that provides an available population of interstitial sites already present in the crystal lattice. To further confirm this scenario and exclude the ion interaction as the cause of higher Na conductivity at a lower temperature, the electric modulus, obtained from EIS, was analyzed in the context of the coupling model (CM).[72] The CM, originally developed to explain the universal dielectric response in glass, polymers, and amorphous compounds, asserts that exists a crossover between Debye-like and non-Debye relaxation process, when the characteristic relaxation time becomes bigger than a critical time (t_c, typically of the order of ps). The main difference between these two regimes is owed to the presence of a dipole−dipole interaction (which is many-body in nature), absent in the Debye model. Mathematically, it consists in replacing the single-body relaxation function $\Phi(t) = e^{-t/\tau_D}$ with the many-body relaxation $\Phi(t) = e^{-(t/\tau*)^{\beta}}$ (also known as the Kohlrausch−Williams−Watts function). Here, τ_D and τ^* are the Debye and CM relaxation time, respectively, while β, that is defined between 0 and 1, is the coupling parameter that measures the strength of the interaction.

To estimate β, we solved the integral in the time domain $M''(\omega) = M_\infty\left[1 + \int_0^\infty \frac{d}{dt}\Phi(t)\, e^{-i\omega t} dt\right]$ (details in the Supporting Information). Figure S7 shows the fitted spectra for pristine and MM-NCB at −50 and −90 °C, respectively. The reason to choose different temperatures lies in the different temperature dependency of the relaxation time. Indeed, for these two measurements, the calculated τ_0 amounts to 4.66 and 3.94 ms, respectively, making the two spectra comparable. The resulting β is 0.66 and 0.6 for NCB and MM-NCB, respectively. This finding is not only in agreement with a similar reported compound by Duchêne et al.[74] but also points out the same interaction process, discarding the ion dynamics as a factor

https://doi.org/10.1021/acsami.1c21113
ACS Appl. Mater. Interfaces XXXX, XXX, XXX−XXX

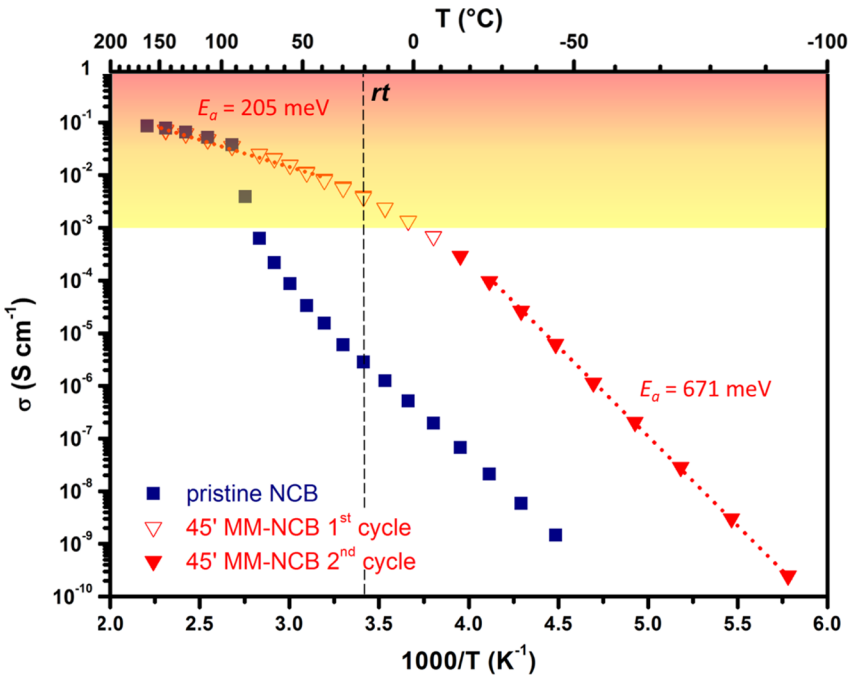

Figure 2. DC conductivity evolution as a function of temperature for pristine (blue squares) and MM-NCB (red triangles). For each temperature, the ionic conductivity was determined from the frequency-independent plateau of the real part of complex conductivity (Figure S5). MM leads to the suppression of the order−disorder phase transition that is noticeable for the nonmilled sample. Nonetheless, the rise in conductivity cannot be ascribable to the grain size reduction. Indeed, a minimal hysteresis between heating and cooling is noticeable, and according to the recrystallization observed after heat treatment during DSC (Figure 1b), σ at a given temperature is unchanged, even though the size of the crystallite domains is augmented. The activation energy is not constant in the whole temperature range and two major Arrhenius behaviors can be noticeable (dotted red lines), with E_a = 205 and 671 meV, respectively. However, although the former region also shows no differences between DC conductivity values between pristine and MM sample, the latter provides σ values which are 4 orders of magnitude larger. Therefore, such difference arises from entropic contributions, being the E_a comparable between milled and nonmilled samples. For the sake of clarity, the superionic regime (σ > 1 mS cm^{-1}) has been highlighted in the graph.

Table 1. a = Lattice Parameter (Cubic Cells), V = Cell Volume, V/Z Normalized Volume Per Formula Unit, Being Z = Number of Formula Units Per Cell (4 and 2 for fcc and bcc, Respectively), ρ = Density, R^- = Anion Crystal Radius[a]

anion packing	a (Å)	V (Å^3)	V/Z (Å^3)	ρ (g cm^{-3})	R^- (Å)	V^- (Å^3)	V^{Na+}/Z (Å^3)
fcc	10.066	1019.9	255.0	1.081	3.56	188.9	66.1
bcc	7.882	489.7	244.8	1.126	3.41	166.0	78.8

[a]The difference between the anion crystal radii of NCB arises from their different packing in fcc and bcc structure, respectively. Indeed, considering these anions as rigid spheres, their radius in each cubic sublattice is calculated according to the respective lattice parameter a, i.e., for fcc anion sublattice, $R^- = \frac{a}{4}\sqrt{2}$, whereas for the bcc $R^- = \frac{a}{4}\sqrt{3}$. R^+/R^- ratio (R^+ = Na^+ radius). V^- = volume of each anion, V^{Na+} = (V-ZV$^-$)/Z, available volume per cation in each NCB polymorph. For simplicity, we consider herein the orthorhombic pseudo-fcc phase as a perfect fcc arrangement, due to the minimal orthorhombic distortion.

improving Na conductivity in the low-temperature range of MM-NCB.

By comparing the Arrhenius plot of the whole sample series (Figure S8), it is worth noting that the increase of conductivity at a given temperature is not linear with the milling time, but it reaches an "optimum" after 45 min of mechanical treatment (Figure S9). Indeed, up to 45 min, MM progressively drives the orthorhombic to bcc phase transition, with a corresponding increase of the bulk conductivity. Beyond such limit, MM is prone to trigger decomposition reactions (further details are discussed below in the Spectroscopy Characterization section) forming nonconductive amorphous phases (Figure S1), becoming predominant in volume and leading to a total conductivity of 10^{-8} S cm^{-1} after 360 min of MM. Finally, it should be also pointed out that 45-min milling does not correspond to a complete formation of conductive bcc phase: Rietveld refinement on the recrystallized MM-NCB (Figure 1b) shows the presence of 8% of orthorhombic NCB. Nonetheless, according to the effective medium model, the bulk conductivity of such sample is driven by the most conducting phase, with the orthorhombic NCB being 4 order of magnitude less conductive than the bcc one.[75] However, the presence of a more resistive phase can be limiting for the interfacial resistance, and opportune tuning of the milling conditions is necessary to achieve a complete phase transformation.

3.1. Factors Affecting Fast Ionic Conductivity in MM-NCB. To deeply understand where the configurational entropy arises from, it is necessary to analyze more in detail the structural changes operated by the mechanical treatment. As a consequence of mechanical milling, the incorporation of defects into the crystalline structure alters its density and atomic coordination, moving the anions from their initial lattice sites, eventually leading to a phase transition toward different packings.[76] For instance, as it has been recently pointed out

https://doi.org/10.1021/acsami.1c21113
ACS Appl. Mater. Interfaces XXXX, XXX, XXX−XXX

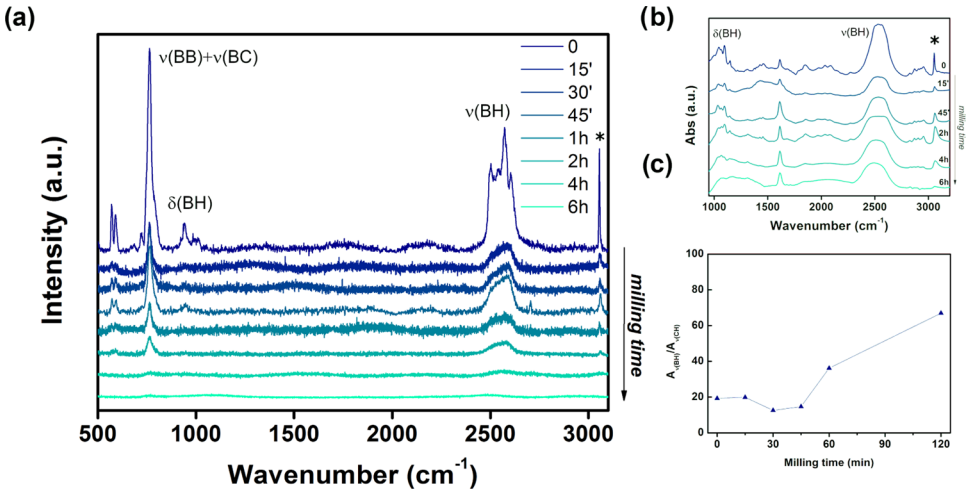

Figure 3. (a) Raman spectra, (b) IR spectra, and (c) ν(BH) to ν(CH) peak area ratio as a function of milling time. Both techniques reveal a rapid broadening of the signal after only 15 min of milling, due to the long-range order loss provoked by MM. Interestingly, a redshift of the ν(BH) signals is also observed as a function of milling time, corresponding to an increased B−H bond distance. However, according to the work of Hagemann et al.,[82] which gives a relation between the bond length r and the IR vibrational frequency ν in several large-cage anions, i.e., $r(\text{Å}) = 1.482 - (1.078 \times 10^{-4}) \times \nu$. Such a shift (from 2525 to 2489 cm^{-1} (dotted line) represents only an increase of ∼0.32% of the B−H bond distance. On the other hand, the ν(CH) peak (3050 cm^{-1}) does not show further shifting as a consequence of the milling. Nonetheless, its integrated signal strongly decreases with respect to that of the multiplet ν(BH) when the NCB powder is milled over more than 1 h. For the sake of clarity, only selected peaks are labeled. A more detailed peak attribution for Raman and IR spectra can be found elsewhere in the literature.[81]

by Famprikis et al., high-energy ball-milling provides mechanical stress that can stabilize a cubic polymorph of Na_3PS_4, which is denser with respect to the thermodynamic tetragonal one.[77] Nonetheless, in the case of MM-NCB, the stabilization of a bcc anion sublattice results in a structure with a less-efficient anion packing, with respect to the pseudo-fcc for the orthorhombic, pristine, NCB, thus allowing ∼15.7% more volume for the cation to move (Table 1).

The mechanism of the transition between (ccp), hexagonal close packing (hcp), and bcc has been long time studied in monoatomic metals, and the orientation relationship between the three packing types has been generalized showing that the transition is of the deformation martensitic type, i.e., requiring only small atomic shifts.[78] The case of ionic compounds with anion packing and cations occupying the interstitial sites, both executing small atomic shifts during the transition, has been studied, for example, in AgI ionic conductor where the transition ccp−bcc was explained by a low-lying optical phonon mode.[79]

However, as it can be argued from Rietveld refinement, such sites are partially occupied in both structures, and Na^+ occupancy differs between the two polymorphs. Indeed, bcc features 24 off-centered tetrahedral and 24 triangular sites and 2 Na^+ per unit cell, resulting in an occupancy of 0.075 of the former and 0.008 of the latter, in agreement with NMR results, whereas fcc has 4 octahedral sites and 4 Na^+ per formula unit, leading to an occupancy of 1. Such difference in the number of possible Na^+ arrangements, i.e., configurational entropy, reflects the flattened energy landscape of the bcc structure with respect to the fcc arrangement, the former providing more favorable cation hopping. Such observations also agree with a previous study dealing with the prominence of the anion packing on the ionic conductivity of *closo*-borates,[73] where the case already observed for both disordered $Li_2B_{12}H_{12}$ (fcc) and $Na_2B_{12}H_{12}$ (bcc) was discussed, the latter being more conductive at a given temperature. It stays to understand why the crystal radius of $CB_{11}H_{12}^-$ anion is smaller in bcc compared to fcc, i.e., why the anion−anion distance is shorter in bcc (Table 1). The response lies in the anion−anion coordination, and the details for an ordered structure are given in the Supporting Information (Figure S10). Whether the same justification of observed denser bcc compared to ccp holds also for disordered structures with dynamic anions stays to be investigated and is an object of our further work. Especially the question of a correlation between the anions rotations could explain why the smaller but simpler triangular bottleneck made of three hydrogens (cf. Figure S10) in bcc results in the same activation energy of Na^+ jumps as a bigger bottleneck of six hydrogens in orthorhombic NCB.

Finally, it is worth mentioning that as a consequence of MM, the formation of hydrogen/sodium defects, which can promote ionic conductivity, cannot be excluded:[43] albeit very rare among *closo*-borates, stable hydrogen-deficient phases have been reported.[80] Nonetheless, if such effect was present, it would be hidden by the main orthorhombic−cubic phase transition, which mostly drives the increase of the ionic conductivity. This is also confirmed by the fact that even the amount of NCB not converted by the mechanical treatment (orthorhombic phase), which undergoes the well-known order−disorder phase transition at around 83 °C, does not dramatically affect the overall conductivity of the MM-NCB. Moreover, further milling leads to samples showing dwindled ionic conductivity, although promoting the formation of amorphous phases (Figures S1 and S7). Unlike that reported for MM-$Li_2B_{12}H_{12}$,[59] from the XPD pattern of the recrystallized NCB, there is neither a peak shift toward low angles nor a change in the relative intensities between (111) and (200) Bragg reflections, which have been indicated as evidence of increased ionic conductivity promoted by hydrogen vacancies (a consequence of the ball-milling).

To get further insight into the changes that the mechanical treatment could have promoted at molecular scale on NCB, Figure 3 shows Raman and IR spectra as a function of milling time. Unlike the icosahedral $[B_{12}H_{12}]^{2-}$, the anion of NCB belongs to the C_{5v} point symmetry group. Therefore, in the stretching region of pristine spectra, it is possible to recognize the splitting of the ν(BH) vibrational modes (2500−2600

https://doi.org/10.1021/acsami.1c21113
ACS Appl. Mater. Interfaces XXXX, XXX, XXX−XXX

500 cm^{-1}), due to the lowered symmetry induced by the presence of
501 the C atom in the $[CB_{11}H_{12}]^-$ cage, as well as the narrow peak at
502 3050 cm^{-1} (C−H stretching).[81] As a first consequence of the
503 mechanical action, the further loss of intensity of all of these
504 peaks can be noticed, with the broadening of the ν(BH) signals,
505 which become indistinguishable after only 15 min of milling.
506 Such a trend, also confirmed by IR spectra, is due to the changes
507 in the surroundings of the $[CB_{11}H_{12}]^-$ ions, promoted by the
508 mechanical action that reduces the size of the crystalline
509 domains and therefore the long-range order.
510 However, the depletion of the signals due to the stretching
511 vibrations is not proportional. Indeed, the ratio between the
512 integrated area of the multiplet of ν(BH) vibrations and that
513 coming from the ν(CH) is not constant as a function of milling
514 time, but is increased by a factor of 3 after 2 h of MM (see Figure
515 3c). This evidence leads to speculate that the mechanical
516 treatment could also provoke a partial dehydrogenation of the
517 complex anion, as already observed for other *closo*-borates,[43]
518 although preferentially occurring at the C, where the more acid
519 bond of the anionic cage is present.[38,63] The bending region
520 (around 900 cm^{-1}) provides an analogous trend as a function of
521 the milling time, with a general broadening of all of the signals.
522 However, due to the convolution of the δ(CH) mode with other
523 vibrations, it is not possible to get more insights from this region
524 of the spectra. Nonetheless, mechanical milling does not seem to
525 lead to degradation reaction involving cage opening, at least up
526 to 2 h of milling time, where both Raman and IR signals are still
527 distinguishable from the baseline since neither evidence of new
528 vibrational modes ascribable to lower-symmetry open-cage *nido*-
529 borates nor further shift of the ν(CH) is found.[81]
530 To establish whether the mechanical treatment has an
531 influence on the electrochemical window, an SSRCV was
f4 532 performed (Figure 4). To assess a reliable oxidative stability for
533 further practical applications,[83] we will refer to the decom-
534 position occurring at the so-called edge potential (E_e), which is

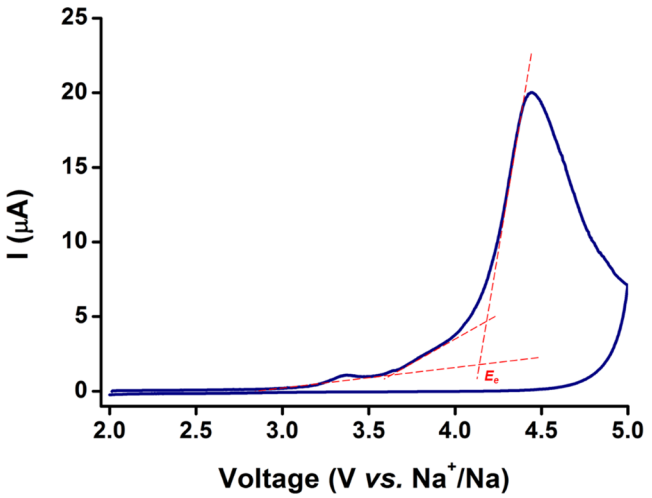

Figure 4. Slow-scan rate cyclic voltammetry of a Na|MM-NCB|Glassy carbon cell. Na is both CE and RE electrode, and glassy carbon is the WE. To enhance the signals coming from the electrochemical reaction, the above layer of the SE pellet was prepared by adding conductive carbon. The measurement was carried out at rt, further increasing the applied potential by 50 μV each second, up to 5 V vs Na^+/Na. The main peak showing an E_e (edge potential) at 4.16 V arises from the oxidation of the MM-NCB. After reversing the voltage scan, no further reduction reactions are noticeable.

the potential where a first faradic current is detectable, and it has 535
been determined according to the literature.[84] 536
After a small anodic peak centered at 3.3 V, already reported in 537
the literature for the nonmilled compound, a major oxidative 538
event is observed, which is not followed by a corresponding 539
cathodic current when the potential scan speed was swapped, 540
thus highlighting an irreversible oxidation of the electrolyte at 541
the working electrode (WE). E_e is 4.14 V, which is in good 542
agreement with previous reports in which the oxidative potential 543
of NCB was found from direct[29] and indirect measurements.[30] It 544
is important to mention that the first oxidative peak, although 545
irreversible, should not impact the practical voltage window of 546
NCB, as it has been reported for a 4 V operating Na-SSB 547
featuring $NaB_{12}H_{12}$-NCB mix as SE.[85] Such findings confirm 548
that the 45-min mechanical treatment enhances the ionic 549
conductivity without altering the oxidative stability of NCB. 550
Figure 5 depicts the evolution of the voltage profile of a 551 f5
symmetric Na|MM-NCB|Na cell over time, operating at rt. To 552

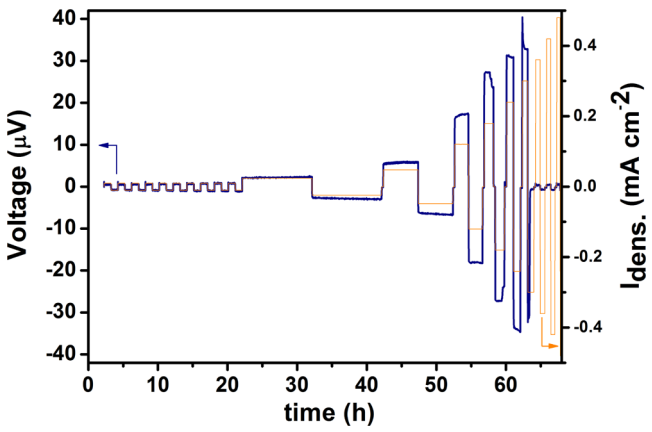

Figure 5. Voltage profile evolution (blue line) of a Na|MM-NCB|Na cell cycled at rt. Each cycle consists of two sweeps in which the current is swapped to reversibly plate and strip sodium on/from the metallic electrodes. After each cycle, the current flowing through the SE is increased (orange line). To keep the amount of Na^+ moving through the SE over further cycles constant, the time length of each sweep is adapted accordingly, i.e., it decreases as the current density is increased. Such a value has been calculated as follows: we consider a positive electrode featuring a specific capacity of 120 mA h g^{-1}, such as $NaCrO_2$, widely employed in Na-SSB prototypes.[92,93] Assuming an electrode loading of 2 mg cm^{-2}, and according to the definition of C/n rate as the current value necessary for the electrode to deliver its whole capacity in n hours, the current density corresponding to 1C is 0.24 mA cm^{-2}.

determine what is the critical current density (CCD) of MM- 553
NCB, the current was further increased after each cycle. CCD 554
has been initially defined as the current density at which the cell 555
potential drops to 0 V.[86] According to that definition, the 556
measured CCD for MM-NCB is 0.3 mA cm^{-2}, where a sudden 557
voltage drop occurs during the second sweep. However, more 558
recent reports agreed with the fact that the current density that 559
leads to the dendrite penetration through the SE is a more 560
appropriate critical parameter to take into account, thus 561
considering that stable cycling can be achieved just below 562
CCD.[87] As shown by Kazyak et al., the dendrite penetration 563
throughout the SE can be detected by thoroughly looking at the 564
galvanostatic cell profile, noticing that a sudden voltage drop can 565
be seen as a reduction of the thickness of the SE.[88] Therefore, 566
according to the first Ohm's law, $V = iR$, such voltage depletion is 567
due to the dendrite penetration, which decreases the effective 568

https://doi.org/10.1021/acsami.1c21113
ACS Appl. Mater. Interfaces XXXX, XXX, XXX−XXX

thickness of the resistive element in the cell. Under such conditions, the cell shortcut due to the dendrite penetration is ineluctable and can only ideally be limited by increasing the thickness of the SE, although depleting the energy density of the cell. According to that more rigorous definition, MM-NCB undergoes dendrite penetration at the current density above 0.12 mA cm^{-2}. Such a value represents the current density necessary to fully charge/discharge a positive electrode gathering a specific capacity of 120 mA h g^{-1}, at the current rate of $C/2$ (see details on the caption of Figure 5). However, it is important to underline that the aforementioned symmetric cell has been cycled without any optimization or control on the stack pressure during cycling. Indeed, several recent reports have shown the pivotal role of pressure control to both limit dendrite penetration during the plating process and reduce the possibility of void formation when Na is stripped.[20,89,90] A thorough study to determine the best stack pressure for maximizing the current density that can flow through MM-NCB, as well as other Ni-based SEs is currently ongoing in our laboratory.[91]

4. CONCLUSIONS

In summary, we report the stabilization at rt of the fast Na^+-conductor bcc polymorph of NCB, obtained via high-energy mechanical milling, using a 3D motion mill, which is a fast, solvent-free, and cost-effective synthetic route. Milling conditions can drive the polymorphism of NCB complex systems: owing to macroscopic stress provided by the mechanical treatment on the powder, it results that a denser structure, although providing better conduction pathways for Na^+ ions, is stabilized after only 15 min of milling. By increasing the milling time, a larger fraction of NCB is further converted into the bcc phase. EIS measurements carried out at different milling times set as an optimum of time maximize the ionic conductivity at 45 min of mechanical treatment, where a σ of 4 mS cm^{-1} at rt is measured. As already observed for other fast ion conductors based on hydroborates, the conductivity of MM-NCB shows a nonlinear evolution over the investigated temperature range. Nonetheless, two Arrhenius regions are detectable: the first one above the transition temperature of nonmilled NCB, where conductivities and activation energy of the milled and nonmilled samples perfectly overlap, and a second one, below rt, where although the activation energy of milled and nonmilled samples matches, the former shows a 4 order of magnitude higher conductivity. Such difference arises from the entropic contribution to the ionic conductivity, which is partly due to the larger number of possible configurations for Na^+ into the bcc lattice. Nonetheless, AIMD simulations are needed to better estimate the difference of available sites between fcc and bcc NCB. Beyond 45-min milling time, further mechanical action likely leads to the chemical degradation of the NCB. Even though further analysis to confirm the possible hydrogen evolution are foreseeable, it can be excluded that the cage opening is a possible decomposition route due to the mechanical action. The MM also does not have an impact on the electrochemical stability of the NCB, which is found to be in line with the previous report on pristine NCB, thus confirming that the reduced particle size does not play a role in the kinetics of the decomposition reactions. Finally, it has been shown that, even though in a nonoptimized system, MM-NCB allows sodium to be reversibly plated/stripped at rt, withstanding decent current densities in comparison with the specific capacities of commonly employed Na-positive electrodes. Such findings prove that the destabilization driving fast ion motion in large-cage hydroborates is not necessarily achieved by further anion mixing, but can be achieved even starting from a unique and cheap precursor,[94] by tuning the stabilization of nonequilibrium disordered phases.

■ ASSOCIATED CONTENT

Supporting Information

The Supporting Information is available free of charge at https://pubs.acs.org/doi/10.1021/acsami.1c21113.

Comparison of X-ray powder patterns, SEM images, and T-dependent ionic conductivities as a function of milling time for pristine and ball-milled samples; DSC scans for 45 min ball-milled sample; structural drawing of bcc polymorph; analysis of anion packing in bcc and ccp polymorphs; and modeling of configurational entropy and dielectric modulus for bcc polymorph (PDF)

■ AUTHOR INFORMATION

Corresponding Author

Radovan Černý − *Laboratory of Crystallography, Department of Quantum Matter Physics, University of Geneva, CH-1211 Geneva, Switzerland;* orcid.org/0000-0002-9847-4372; Email: radovan.cerny@unige.ch

Authors

Fabrizio Murgia − *Laboratory of Crystallography, Department of Quantum Matter Physics, University of Geneva, CH-1211 Geneva, Switzerland*

Matteo Brighi − *Laboratory of Crystallography, Department of Quantum Matter Physics, University of Geneva, CH-1211 Geneva, Switzerland*

Laura Piveteau − *Institute of Chemical Sciences and Engineering, NMR Platform, Ecole Polytechnique Fédérale de Lausanne, CH-1015 Lausanne, Switzerland*

Claudia E. Avalos − *Institute of Chemical Sciences and Engineering, NMR Platform, Ecole Polytechnique Fédérale de Lausanne, CH-1015 Lausanne, Switzerland;* Present Address: Department of Chemistry, New York University, New York, New York 10003, United States

Valerio Gulino − *Materials Chemistry and Catalysis, Debye Institute for Nanomaterials Science, Utrecht University, 3584 CG Utrecht, The Netherlands*

Marc C. Nierstenhöfer − *Fakultät für Mathematik und Naturwissenschaften, Anorganische Chemie, Bergische Universität Wuppertal, 42119 Wuppertal, Germany*

Peter Ngene − *Materials Chemistry and Catalysis, Debye Institute for Nanomaterials Science, Utrecht University, 3584 CG Utrecht, The Netherlands;* orcid.org/0000-0003-3691-0623

Petra de Jongh − *Materials Chemistry and Catalysis, Debye Institute for Nanomaterials Science, Utrecht University, 3584 CG Utrecht, The Netherlands;* orcid.org/0000-0002-2216-2620

Complete contact information is available at: https://pubs.acs.org/10.1021/acsami.1c21113

Author Contributions

The manuscript was written through contributions of all authors. All authors have given approval to the final version of the manuscript.

https://doi.org/10.1021/acsami.1c21113
ACS Appl. Mater. Interfaces XXXX, XXX, XXX−XXX

Funding

F.M., M.B., and R.C. received funding from the University of Geneva.

Notes

The authors declare no competing financial interest.

■ ACKNOWLEDGMENTS

The authors acknowledge Dr. Jeremie Teyssier (UNIGE) for the Raman measurements, as well as Prof. Hans Hagemann (UNIGE) for the fruitful discussion on the interpretation of IR spectra. Dr. Pascal Schouwink (EPFL) is acknowledged for the test with a collection of XPD patterns with high-intensity setup.

■ ABBREVIATION

NASICON, Na superionic conductor

■ REFERENCES

(1) Hasa, I.; Mariyappan, S.; Saurel, D.; Adelhelm, P.; Koposov, A. Y.; Masquelier, C.; Croguennec, L.; Casas-Cabanas, M. Challenges of Today for Na-Based Batteries of the Future: From Materials to Cell Metrics. *J. Power Sources* **2021**, *482*, No. 228872.

(2) Ferrari, S.; Falco, M.; Muñoz-García, A. B.; Bonomo, M.; Brutti, S.; Pavone, M.; Gerbaldi, C. Solid-State Post Li Metal Ion Batteries: A Sustainable Forthcoming Reality? *Adv. Energy Mater.* **2021**, No. 2100785.

(3) Vaalma, C.; Buchholz, D.; Weil, M.; Passerini, S. A Cost and Resource Analysis of Sodium-Ion Batteries Electronics. *Nat. Rev. Mater.* **2018**, *3*, No. 18013.

(4) Zhao, C.; Liu, L.; Qi, X.; Lu, Y.; Wu, F.; Zhao, J.; Yu, Y.; Hu, Y. S.; Chen, L. Solid-State Sodium Batteries. *Adv. Energy Mater.* **2018**, *8*, No. 1703012.

(5) Crabtree, G. The Coming Electric Vehicle Transformation. *Science* **2019**, *366*, 422−424.

(6) Chen, R.; Li, Q.; Yu, X.; Chen, L.; Li, H. Approaching Practically Accessible Solid-State Batteries: Stability Issues Related to Solid Electrolytes and Interfaces. *Chem. Rev.* **2020**, *120*, 6820−6877.

(7) Zhang, Z.; Shao, Y.; Lotsch, B.; Hu, Y. S.; Li, H.; Janek, J.; Nazar, L. F.; Nan, C. W.; Maier, J.; Armand, M.; Chen, L. New Horizons for Inorganic Solid State Ion Conductors. *Energy Environ. Sci.* **2018**, *11*, 1945−1976.

(8) Janek, J.; Zeier, W. G. A Solid Future for Battery Development. *Nat. Energy* **2016**, *1*, No. 16141.

(9) Deng, J.; Bae, C.; Denlinger, A.; Miller, T. Electric Vehicles Batteries: Requirements and Challenges. *Joule* **2020**, *4*, 511−515.

(10) Schnell, J.; Knörzer, H.; Imbsweiler, A. J.; Reinhart, G. Solid versus Liquid—A Bottom-Up Calculation Model to Analyze the Manufacturing Cost of Future High-Energy Batteries. *Energy Technol.* **2020**, *8*, No. 1901237.

(11) *A New Breed of Battery - Investor Presentation*; Solid Power: Louisville, 2021. https://s28.q4cdn.com/717221730/files/doc_presentations/Solid-Power-Investor-Presentation-June-2021-Final.pdf.

(12) Kamaya, N.; Homma, K.; Yamakawa, Y.; Hirayama, M.; Kanno, R.; Yonemura, M.; Kamiyama, T.; Kato, Y.; Hama, S.; Kawamoto, K.; Mitsui, A. A Lithium Superionic Conductor. *Nat. Mater.* **2011**, *10*, 682−686.

(13) Dehnen, S.; Duchardt, M.; Roling, B.; Ruschewitz, U.; Adams, S. Vacancy-Controlled Na+ Superion Conduction in Na11Sn2PS12. *Angew. Chem., Int. Ed.* **2018**, *57*, 1351−1355.

(14) Park, K. H.; Bai, Q.; Kim, D. H.; Oh, D. Y.; Zhu, Y.; Mo, Y.; Jung, Y. S. Design Strategies, Practical Considerations, and New Solution Processes of Sulfide Solid Electrolytes for All-Solid-State Batteries. *Adv. Energy Mater.* **2018**, *8*, No. 1800035.

(15) Hayashi, A.; Masuzawa, N.; Yubuchi, S.; Tsuji, F.; Hotehama, C.; Sakuda, A.; Tatsumisago, M. A Sodium-Ion Sulfide Solid Electrolyte with Unprecedented Conductivity at Room Temperature. *Nat. Commun.* **2019**, *10*, No. 5266.

(16) Randau, S.; Weber, D. A.; Kötz, O.; Koerver, R.; Braun, P.; Weber, A.; Ivers-Tiffée, E.; Adermann, T.; Kulisch, J.; Zeier, W. G.; Richter, F. H.; Janek, J. Benchmarking the Performance of All-Solid-State Lithium Batteries. *Nat. Energy* **2020**, *5*, 259−270.

(17) Famprikis, T.; Canepa, P.; Dawson, J. A.; Islam, M. S.; Masquelier, C. Fundamentals of Inorganic Solid-State Electrolytes for Batteries. *Nat. Mater.* **2019**, *18*, 1278−1291.

(18) Singer, C.; Schnell, J.; Reinhart, G. Scalable Processing Routes for the Production of All-Solid-State Batteries—Modeling Interdependencies of Product and Process. *Energy Technol.* **2021**, *9*, No. 2000665.

(19) Wang, M. J.; Choudhury, R.; Sakamoto, J. Characterizing the Li-Solid-Electrolyte Interface Dynamics as a Function of Stack Pressure and Current Density. *Joule* **2019**, *3*, 2165−2178.

(20) Doux, J. M.; Nguyen, H.; Tan, D. H. S.; Banerjee, A.; Wang, X.; Wu, E. A.; Jo, C.; Yang, H.; Meng, Y. S. Stack Pressure Considerations for Room-Temperature All-Solid-State Lithium Metal Batteries. *Adv. Energy Mater.* **2020**, *10*, No. 1903253.

(21) Hayashi, A.; Noi, K.; Sakuda, A.; Tatsumisago, M. Superionic Glass-Ceramic Electrolytes for Room-Temperature Rechargeable Sodium Batteries. *Nat. Commun.* **2012**, *3*, No. 856.

(22) Wang, H.; Chen, Y.; Hood, Z. D.; Sahu, G.; Pandian, A. S.; Keum, J. K.; An, K.; Liang, C. An Air-Stable Na3SbS4Superionic Conductor Prepared by a Rapid and Economic Synthetic Procedure. *Angew. Chem., Int. Ed.* **2016**, *55*, 8551−8555.

(23) Tian, Y.; Shi, T.; Richards, W. D.; Li, J.; Kim, J. C.; Bo, S.-H.; Ceder, G. Compatibility Issues between Electrodes and Electrolytes in Solid-State Batteries. *Energy Environ. Sci.* **2017**, *10*, 1150−1166.

(24) Lacivita, V.; Wang, Y.; Bo, S.-H.; Ceder, G. Ab Initio Investigation of the Stability of Electrolyte/Electrode Interfaces in All-Solid-State Na Batteries. *J. Mater. Chem. A* **2019**, *7*, 8144−8155.

(25) Sun, Y.; Wang, Y.; Liang, X.; Xia, Y.; Peng, L.; Jia, H.; Li, H.; Bai, L.; Feng, J.; Jiang, H.; Xie, J. Rotational Cluster Anion Enabling Superionic Conductivity in Sodium-Rich Antiperovskite Na3OBH4. *J. Am. Chem. Soc.* **2019**, *141*, 5640−5644.

(26) Ahiavi, E.; Dawson, J. A.; Kudu, U.; Courty, M.; Islam, M. S.; Clemens, O.; Masquelier, C.; Famprikis, T. Mechanochemical Synthesis and Ion Transport Properties of Na3OX (X = Cl, Br, I and BH4) Antiperovskite Solid Electrolytes. *J. Power Sources* **2020**, *471*, No. 228489.

(27) Matsuo, M.; Nakamori, Y.; Orimo, S. I.; Maekawa, H.; Takamura, H. Lithium Superionic Conduction in Lithium Borohydride Accompanied by Structural Transition. *Appl. Phys. Lett.* **2007**, *91*, No. 224103.

(28) Le Ruyet, R.; Berthelot, R.; Salager, E.; Florian, P.; Fleutot, B.; Janot, R. Investigation of Mg(BH4)(NH2)-Based Composite Materials with Enhanced Mg2+ Ionic Conductivity. *J. Phys. Chem. C* **2019**, *123*, 10756−10763.

(29) Asakura, R.; Duchêne, L.; Kühnel, R. S.; Remhof, A.; Hagemann, H.; Battaglia, C. Electrochemical Oxidative Stability of Hydroborate-Based Solid-State Electrolytes. *ACS Appl. Energy Mater.* **2019**, *2*, 6924−6930.

(30) Brighi, M.; Murgia, F.; Cerny, R. Closo -Hydroborate Sodium Salts as an Emerging Class of Room-Temperature Solid Electrolytes Closo -Hydroborate Sodium Salts as an Emerging Class of Room-Temperature Solid Electrolytes. *Cell Rep. Phys. Sci.* **2020**, *1*, No. 100217.

(31) Černý, R.; Brighi, M.; Murgia, F. The Crystal Chemistry of Inorganic Hydroborates. *Chemistry* **2020**, *2*, 805−826.

(32) Brighi, M.; Murgia, F.; Łodziana, Z.; Schouwink, P.; Wołczyk, A.; Černý, R. A Mixed Anion Hydroborate/Carba-Hydroborate as a Room Temperature Na-Ion Solid Electrolyte. *J. Power Sources* **2018**, *404*, 7−12.

(33) Kim, S.; Oguchi, H.; Toyama, N.; Sato, T.; Takagi, S.; Otomo, T.; Arunkumar, D.; Kuwata, N.; Kawamura, J.; Orimo, S. A Complex Hydride Lithium Superionic Conductor for High-Energy-Density All-Solid-State Lithium Metal Batteries. *Nat. Commun.* **2019**, *10*, No. 1081.

(34) Mohtadi, R.; Orimo, S. The Renaissance of Hydrides as Energy Materials. *Nat. Rev. Mater.* **2016**, *2*, No. 16091.

https://doi.org/10.1021/acsami.1c21113
ACS Appl. Mater. Interfaces XXXX, XXX, XXX−XXX

(35) Douvris, C.; Michl, J. Chemistry of the Carba-Closo-Dodecaborate(-) Anion, CB11H12-. *Chem. Rev.* **2013**, *113*, PR179−PR233.
(36) Lu, Z.; Ciucci, F. Metal Borohydrides as Electrolytes for Solid-State Li, Na, Mg, and Ca Batteries: A First-Principles Study. *Chem. Mater.* **2017**, *29*, 9308−9319.
(37) Varley, J. B.; Kweon, K.; Mehta, P.; Shea, P.; Heo, T. W.; Udovic, T. J.; Stavila, V.; Wood, B. C. Understanding Ionic Conductivity Trends in Polyborane Solid Electrolytes from Ab Initio Molecular Dynamics. *ACS Energy Lett.* **2017**, *2*, 250−255.
(38) Dimitrievska, M.; Shea, P.; Kweon, K. E.; Bercx, M.; Varley, J. B.; Tang, W. S.; Skripov, A. V.; Stavila, V.; Udovic, T. J.; Wood, B. C. Carbon Incorporation and Anion Dynamics as Synergistic Drivers for Ultrafast Diffusion in Superionic LiCB11H12 and NaCB11H12. *Adv. Energy Mater.* **2018**, *8*, No. 1703422.
(39) Verdal, N.; Udovic, T. J.; Stavila, V.; Tang, W. S.; Rush, J. J.; Skripov, A. V. Anion Reorientations in the Superionic Conducting Phase of Na 2B12H12. *J. Phys. Chem. C* **2014**, *118*, 17483−17489.
(40) Skripov, A. V.; Skoryunov, R. V.; Soloninin, A. V.; Babanova, O. A.; Stavila, V.; Udovic, T. J. Nuclear Magnetic Resonance Study of Anion and Cation Reorientational Dynamics in (NH4)2B12H12. *J. Phys. Chem. C* **2018**, *122*, 3256−3262.
(41) Soloninin, A. V.; Skoryunov, R. V.; Babanova, O. A.; Skripov, A. V.; Dimitrievska, M.; Udovic, T. J. Comparison of Anion and Cation Dynamics in a Carbon-Substituted Closo-Hydroborate Salt: 1H and 23Na NMR Studies of Solid-Solution Na2(CB9H10)(CB11H12). *J. Alloys Compd.* **2019**, *800*, 247−253.
(42) Timmermans, J. Plastic Crystals: A Historical Overview. *J. Phys. Chem. Solids* **1961**, *18*, 1−8.
(43) Kim, S.; Toyama, N.; Oguchi, H.; Sato, T.; Takagi, S.; Ikeshoji, T.; Orimo, S. Fast Lithium-Ion Conduction in Atom-Deficient *Closo* -Type Complex Hydride Solid Electrolytes. *Chem. Mater.* **2018**, 386−391.
(44) Sadikin, Y.; Schouwink, P.; Brighi, M.; Zbigniew, Ł.; Radovan, C. Modified Anion Packing of Na2B12 H12 in Close to Room Temperature Superionic Conductors. *Inorg. Chem.* **2017**, *56*, 5006−5016.
(45) Tang, W. S.; Yoshida, K.; Soloninin, A. V.; Skoryunov, R. V.; Babanova, O. A.; Skripov, A. V.; Dimitrievska, M.; Stavila, V.; Orimo, S.; Udovic, T. J. Stabilizing Superionic-Conducting Structures via Mixed-Anion Solid Solutions of Monocarba- Closo -Borate Salts. *ACS Energy Lett.* **2016**, *1*, 659−664.
(46) Gulino, V.; Brighi, M.; Murgia, F.; Ngene, P.; de Jongh, P.; Černý, R.; Baricco, M. Room-Temperature Solid-State Lithium-Ion Battery Using a LiBH 4 −MgO Composite Electrolyte. *ACS Appl. Energy Mater.* **2021**, *4*, 1228−1236.
(47) Zettl, R.; De Kort, L.; Gombotz, M.; Wilkening, H. M. R.; De Jongh, P. E.; Ngene, P. Combined Effects of Anion Substitution and Nanoconfinement on the Ionic Conductivity of Li-Based Complex Hydrides. *J. Phys. Chem. C* **2020**, *124*, 2806−2816.
(48) Suryanarayana, C. Mechanical Alloying and Milling. *Prog. Mater. Sci.* **2001**, *46*, 1−184.
(49) Gaffet, E.; Le Caër, G. Mechanical Milling. In *Nanomaterials and Nanochemistry*; Bréchignac, C.; Houdy, P. L. M., Eds.; Springer: Berlin, Heidelberg, 2008; pp 455−471.
(50) Delogu, F.; Mulas, G.; Schiffini, L.; Cocco, G. Mechanical Work and Conversion Degree in Mechanically Induced Processes. *Mater. Sci. Eng. A* **2004**, *382*, 280−287.
(51) Humphry-Baker, S. A.; Garroni, S.; Delogu, F.; Schuh, C. A. Melt-Driven Mechanochemical Phase Transformations in Moderately Exothermic Powder Mixtures. *Nat. Mater.* **2016**, *15*, 1280−1286.
(52) Schlem, R.; Muy, S.; Prinz, N.; Banik, A.; Shao-Horn, Y.; Zobel, M.; Zeier, W. G. Mechanochemical Synthesis: A Tool to Tune Cation Site Disorder and Ionic Transport Properties of Li3MCl6 (M = Y, Er) Superionic Conductors. *Adv. Energy Mater.* **2020**, *10*, No. 1903719.
(53) Liu, D.; Lei, W.; Qin, S.; Hou, L.; Liu, Z.; Cui, Q.; Chen, Y. Large-Scale Synthesis of Hexagonal Corundum-Type In2O 3 by Ball Milling with Enhanced Lithium Storage Capabilities. *J. Mater. Chem. A* **2013**, *1*, 5274−5278.
(54) Gaffet, E.; Yousfi, L. Crystal to Non-Equilibrium Phase Transition Induced by Ball-Milling. *Mater. Sci. Forum* **1992**, *88−90*, 51−58.
(55) Calka, A. Formation of Titanium and Zirconium Nitrides by Mechanical Alloying. *Appl. Phys. Lett.* **1991**, *59*, 1568−1569.
(56) Napolitano, E.; Mulas, G.; Enzo, S.; Delogu, F. Kinetics of Mechanically Induced Anatase-to-Rutile Phase Transformations under Inelastic Impact Conditions. *Acta Mater.* **2010**, *58*, 3798−3804.
(57) Garroni, S.; Milanese, C.; Pottmaier, D.; Mulas, G.; Nolis, P.; Girella, A.; Caputo, R.; Olid, D.; Teixdor, F.; Baricco, M.; Marini, A.; Suriñach, S.; Baró, M. D. Experimental Evidence of Na2[B12H12] and Na Formation in the Desorption Pathway of the 2NaBH4 + MgH 2 System. *J. Phys. Chem. C* **2011**, *115*, 16664−16671.
(58) Teprovich, J. A.; Colón-Mercado, H.; Washington, A. L.; Ward, P. A.; Greenway, S.; Missimer, D. M.; Hartman, H.; Velten, J.; Christian, J. H.; Zidan, R. Bi-Functional Li2B12H12 for Energy Storage and Conversion Applications: Solid-State Electrolyte and Luminescent down-Conversion Dye. *J. Mater. Chem. A* **2015**, *3*, 22853−22859.
(59) Tang, W. S.; Matsuo, M.; Wu, H.; Stavila, V.; Unemoto, A.; Orimo, S. I.; Udovic, T. J. Stabilizing Lithium and Sodium Fast-Ion Conduction in Solid Polyhedral-Borate Salts at Device-Relevant Temperatures. *Energy Storage Mater.* **2016**, *4*, 79−83.
(60) Favre-Nicolin, V.; Černý, R. FOX, "Free Objects for Crystallography": A Modular Approach to Ab Initio Structure Determination from Powder Diffraction. *J. Appl. Crystallogr.* **2002**, *35*, 734−743.
(61) Coelho, A. A. Whole-Profile Structure Solution from Powder Diffraction Data Using Simulated Annealing. *J. Appl. Crystallogr.* **2000**, *33*, 899−908.
(62) Hayashi, S.; Hayamizu, K. Accurate Determination of NMR Chemical Shifts in Alkali Halides and Their Correlation with Structural Factors. *Bull. Chem. Soc. Jpn.* **1990**, 913−919.
(63) Tang, W. S.; Unemoto, A.; Zhou, W.; Stavila, V.; Matsuo, M.; Wu, H.; Orimo, S. I.; Udovic, T. J. Unparalleled Lithium and Sodium Superionic Conduction in Solid Electrolytes with Large Monovalent Cage-like Anions. *Energy Environ. Sci.* **2015**, *8*, 3637−3645.
(64) Verdal, N.; Her, J. H.; Stavila, V.; Soloninin, A. V.; Babanova, O. A.; Skripov, A. V.; Udovic, T. J.; Rush, J. J. Complex High-Temperature Phase Transitions in Li2B 12H12 and Na2B12H12. *J. Solid State Chem.* **2014**, *212*, 81−91.
(65) Huot, J.; Liang, G.; Boily, S.; Van Neste, A.; Schulz, R. Structural Study and Hydrogen Sorption Kinetics of Ball-Milled Magnesium Hydride. *J. Alloys Compd.* **1999**, *293−295*, 495−500.
(66) Djilali, Z.; Said, B. Study of the Ball Milling Device for Synthesizing Nanocrystalline Powder. *J. Nano Res.* **2017**, *47*, 60−70.
(67) Germann, L. S.; Arhangelskis, M.; Etter, M.; Dinnebier, R. E.; Friščić, T. Challenging the Ostwald Rule of Stages in Mechanochemical Cocrystallisation. *Chem. Sci.* **2020**, *11*, 10092−10100.
(68) Carrillo, A.; Escoda, L.; Saurina, J.; Suñol, J. J. Structural and Magnetic Behavior of Fe(Nb,Zr) Rich Alloys Produced by Mechanical Alloying. *AIP Adv.* **2018**, *8*, No. 047704.
(69) Blanchard, D.; Nale, A.; Dadi, S.; Eggenhuisen, T. M.; Verkuijlen, M. H. W.; Suwarno; Vegge, T.; Kentgens, A. P. M.; De Jongh, P. E. Nanoconfined LiBH4 as a Fast Lithium Ion Conductor. *Adv. Funct. Mater.* **2015**, *25*, 184−192.
(70) Tang, W. S.; Matsuo, M.; Wu, H.; Stavila, V.; Zhou, W.; Talin, A. A.; Soloninin, A. V.; Skoryunov, R. V.; Babanova, O. A.; Skripov, A. V.; Unemoto, A.; Orimo, S.-I.; Udovic, T. J. Liquid-Like Ionic Conduction in Solid Lithium and Sodium Monocarba- Closo -Decaborates Near or at Room Temperature. *Adv. Energy Mater.* **2016**, *6*, No. 1502237.
(71) Marple, M. A. T.; Aitken, B. G.; Kim, S.; Sen, S. Observation of a Phonon Softening Effect on Li Ion Conduction in Mixed-Anion Chalcogenide Glasses. *Chem. Mater.* **2018**, *30*, 5896−5903.
(72) Duan, S.; Huang, C.; Liu, M.; Cao, Z.; Tian, X.; Hou, S.; Li, J.; Huang, B.; Jin, H. Competition between Activation Energy and Migration Entropy in Lithium Ion Conduction in Superionic NASICON-Type Li1−3xGaxZr2(PO4)3. *J. Mater. Chem. A* **2021**, *9*, 7817−7825.

https://doi.org/10.1021/acsami.1c21113
ACS Appl. Mater. Interfaces XXXX, XXX, XXX−XXX

(73) Kweon, K. E.; Varley, J. B.; Shea, P.; Adelstein, N.; Mehta, P.; Heo, T. W.; Udovic, T. J.; Stavila, V.; Wood, B. C. Structural, Chemical, and Dynamical Frustration: Origins of Superionic Conductivity in Closo-Borate Solid Electrolytes. *Chem. Mater.* **2017**, *29*, 9142−9153.
(74) Duchêne, L.; Lunghammer, S.; Burankova, T.; Liao, W. C.; Embs, J. P.; Copéret, C.; Wilkening, H. M. R.; Remhof, A.; Hagemann, H.; Battaglia, C. Ionic Conduction Mechanism in the Na 2 (B 12 H 12) 0.5 (B 10 H 10) 0.5 Closo-Borate Solid-State Electrolyte: Interplay of Disorder and Ion-Ion Interactions. *Chem. Mater.* **2019**, *31*, 3449−3460.
(75) Barsoukov, E.; Macdonald, J. R. *Impedance Spectroscopy Theory, Experiment, and Applications*, 2nd ed.; John Wiley & Sons: Hoboken, NJ, 2005.
(76) Gleiter, H. Nanocyrstalline Materials. *Prog. Mater. Sci.* **1989**, *33*, 223−315.
(77) Famprikis, T.; Kudu, O. U.; Dawson, J. A.; Canepa, P.; Fauth, F.; Suard, E.; Zbiri, M.; Dambournet, D.; Borkiewicz, O. J.; Bouyanfif, H.; Emge, S. P.; Cretu, S.; Chotard, J. N.; Grey, C. P.; Zeier, W. G.; Islam, M. S.; Masquelier, C. Under Pressure: Mechanochemical Effects on Structure and Ion Conduction in the Sodium-Ion Solid Electrolyte Na3PS4. *J. Am. Chem. Soc.* **2020**, *142*, 18422−18436.
(78) Cayron, C. Angular Distortive Matrices of Phase Transitions in the Fcc-Bcc-Hcp System. *Acta Mater.* **2016**, *111*, 417−441.
(79) Bührer, W.; Brüesch, P. Phonon Dispersion and B→α Transition in Silver Iodide. *Solid State Commun.* **1975**, *16*, 155−158.
(80) Paskevicius, M.; Pitt, M. P.; Brown, D. H.; Sheppard, D. A.; Chumphongphan, S.; Buckley, C. E. First-Order Phase Transition in the Li2B12H 12 System. *Phys. Chem. Chem. Phys.* **2013**, *15*, 15825−15828.
(81) Kononova, E. G.; Bukalov, S. S.; Leites, L. A.; Lyssenko, K. A.; Ol'shevskaya, V. A. Vibrational Spectra and Structure of Cesium Salts of Icosahedral Monocarba Closo Dodecarborate Anion, [CB11H12]−, and Its Nido Derivative, [CB10H13]−. *Russ. Chem. Bull.* **2003**, *52*, 85−92.
(82) Hagemann, H.; Sharma, M.; Sethio, D.; Lawson Daku, L. M. Correlating Boron−Hydrogen Stretching Frequencies with Boron−Hydrogen Bond Lengths in Closoboranes: An Approach Using DFT Calculations. *Helv. Chim. Acta* **2018**, *101*, No. e1700239.
(83) Gulino, V.; Brighi, M.; Dematteis, E. M.; Murgia, F.; Nervi, C.; Černý, R.; Baricco, M. Phase Stability and Fast Ion Conductivity in the Hexagonal LiBH 4 −LiBr−LiCl Solid Solution. *Chem. Mater.* **2019**, *31*, 5133−5144.
(84) Espinoza, E. M.; Clark, J. A.; Soliman, J.; Derr, J. B.; Morales, M.; Vullev, V. I. Practical Aspects of Cyclic Voltammetry: How to Estimate Reduction Potentials When Irreversibility Prevails. *J. Electrochem. Soc.* **2019**, *166*, H3175−H3187.
(85) Asakura, R.; Reber, D.; Duchêne, L.; Payandeh, S.; Remhof, A.; Hagemann, H.; Battaglia, C. 4 V Room-Temperature All-Solid-State Sodium Battery Enabled by a Passivating Cathode/Hydroborate Solid Electrolyte Interface. *Energy Environ. Sci.* **2020**, *13*, 5048−5058.
(86) Sharafi, A.; Meyer, H. M.; Nanda, J.; Wolfenstine, J.; Sakamoto, J. Characterizing the Li-Li7La3Zr2O12 Interface Stability and Kinetics as a Function of Temperature and Current Density. *J. Power Sources* **2016**, *302*, 135−139.
(87) Taylor, N. J.; Stangeland-Molo, S.; Haslam, C. G.; Sharafi, A.; Thompson, T.; Wang, M.; Garcia-Mendez, R.; Sakamoto, J. Demonstration of High Current Densities and Extended Cycling in the Garnet Li7La3Zr2O12 Solid Electrolyte. *J. Power Sources* **2018**, *396*, 314−318.
(88) Kazyak, E.; Garcia-Mendez, R.; LePage, W. S.; Sharafi, A.; Davis, A. L.; Sanchez, A. J.; Chen, K. H.; Haslam, C.; Sakamoto, J.; Dasgupta, N. P. Li Penetration in Ceramic Solid Electrolytes: Operando Microscopy Analysis of Morphology, Propagation, and Reversibility. *Matter* **2020**, *2*, 1025−1048.
(89) Tu, Q.; Barroso-Luque, L.; Shi, T.; Ceder, G. Electrodeposition and Mechanical Stability at Lithium-Solid Electrolyte Interface during Plating in Solid-State Batteries. *Cell Rep. Phys. Sci.* **2020**, *1*, No. 100106.
(90) Wang, M. J.; Chang, J. Y.; Wolfenstine, J. B.; Sakamoto, J. Analysis of Elastic, Plastic, and Creep Properties of Sodium Metal and Implications for Solid-State Batteries. *Materialia* **2020**, *12*, No. 100792.
(91) Brighi, M.; Murgia, F.; Černý, R. Mechanical Behavior and Dendrite Resistance of Closo -Hydroborate Solid Electrolyte. *Adv. Mater. Interfaces* **2021**, No. 2101254.
(92) Duchêne, L.; Kühnel, R.-S.; Stilp, E.; Cuervo Reyes, E.; Remhof, A.; Hagemann, H.; Battaglia, C. A Stable 3 V All-Solid-State Sodium−Ion Battery Based on a Closo -Borate Electrolyte. *Energy Environ. Sci.* **2017**, *10*, 2609−2615.
(93) Murgia, F.; Brighi, M.; Černý, R. Room-Temperature-Operating Na Solid-State Battery with Complex Hydride as Electrolyte. *Electrochem. Commun.* **2019**, *106*, No. 106534.
(94) Berger, A.; Buckley, C. E.; Paskevicius, M. Synthesis of Closo -CB 11 H 12 − Salts Using Common Laboratory Reagents. *Inorg. Chem.* **2021**, 14744−14751.

https://doi.org/10.1021/acsami.1c21113
ACS Appl. Mater. Interfaces XXXX, XXX, XXX−XXX